Continuous-wave room-temperature diamond maser

Jonathan D. Breeze,[1,2,*] Enrico Salvadori,[3,4,5] Juna Sathian,[1]
Neil McN. Alford,[1,2] and Christopher W.M. Kay[3,4,6]

[1]*Department of Materials, Imperial College London, Exhibition Road, London, SW7 2AZ, UK.*

[2]*London Centre for Nanotechnology, Imperial College London, Exhibition Road, London, SW7 2AZ, UK.*

[3]*Institute of Structural & Molecular Biology, University College London, Gower Street, London, WC1E 8BT, UK.*

[4]*London Centre for Nanotechnology, 17-19 Gordon Street, London, WC1H 0AH, UK.*

[5]*School of Biological and Chemical Sciences, Queen Mary University of London, Mile End Road, London, E1 4NS, UK.*

[6]*Department of Chemistry, University of Saarland, 66123 Saarbrücken, Germany.*

The maser, older sibling of the laser, has been confined to relative obscurity due to its reliance on cryogenic refrigeration and high-vacuum systems. Despite this it has found application in deep-space communications and radio astronomy due to its unparalleled performance as a low-noise amplifier and oscillator. The recent demonstration of a room-temperature solid-state maser exploiting the photo-excited triplet state of pentacene molecules in a p-terphenyl host [1–3] paves the way for a new class of maser. However, to date, only pulsed operation has been observed in this system. The p-terphenyl host has poor thermal and mechanical properties, and the triplet sub-level decay rates of pentacene make continuous emission challenging: alternative materials are therefore required. Hence, inorganic materials containing spin-defects such as diamond [4–6] and silicon carbide [7] have been proposed. Here we report a continuous-wave (CW) room-temperature maser oscillator using optically pumped nitrogen-vacancy (NV^-) defect centres in diamond. This demonstration unlocks the potential of room-temperature solid-state masers for use in a new generation of microwave devices that could find applications in medicine, security and sensing

* jonathan.breeze@imperial.ac.uk

Solid-state masers, developed in the 1960s, were realised by pumping paramagnetic impurity spin states, for example Cr^{3+} ions doped into single-crystal sapphire (ruby). Pumping three-level systems with microwaves generates a population inversion — the requisite feature for amplification by stimulated emission in both masers and lasers, where a higher energy state is more populated than a lower energy state.

The first demonstration of a room-temperature solid-state maser required over 200 W of optical power to overcome the masing threshold, producing a burst of microwave power at 1.45 GHz [1]. This maser was subsequently improved and miniaturised using strontium titanate as the dielectric resonator material [2, 3], lowering the optical pump threshold and volume by two orders of magnitude. However, the threshold pump rate per molecule remained the same at $\sim 10^4$ s^{-1}. Hence, even if CW operation could be achieved in organic triplet-based masers, since almost all the absorbed optical pump power generates heat through non-radiative relaxation processes, thermal runaway is a serious problem since the thermal properties of organic hosts are poor. For example, the pentacene host *p*-terphenyl has a very low thermal conductivity of 0.1 $Wm^{-1}K^{-1}$ and melting point of 230 °C.

Inorganic materials offer superior thermal and mechanical properties compared to organic materials. Specifically, those hosting spin defects offer a potential route to realising CW room-temperature solid-state masers if the population of the defect spin states can be polarised (inverted). Silicon carbide (SiC) is a promising candidate whose various types of spin-defect can be individually addressed by tuning the wavelength of optical excitation and externally applied magnetic field, which, through the Zeeman interaction, can select specific spin multiplicities. V_{Si} defects have spin-quadruplet ground-states which can be polarised through optical pumping. Continuous stimulated emission of microwaves from optically pumped silicon vacancy (V_{Si}) defects in 6H-SiC has recently been reported [7], but masing remained elusive.

In the 1960s, nitrogen impurities in diamond were proposed as potential maser gain media [8–10], using a four-spin flip cross-relaxation mechanism to produce a population inversion in paramagnetic spin-$\frac{1}{2}$ nitrogen donors. Charged nitrogen-vacancy (NV^-) defect centres in diamond (see Fig. 1a) were observed using electron paramagnetic resonance (EPR) almost 40 years ago [11]. The ability to prepare and read the quantum state of the triplet sub-levels efficiently using optically detected magnetic resonance has enabled applications of NV^- centres in magnetometry [12–14] and quantum information processing

[15]. They were recently proposed as quantum emitters for room-temperature masers [6] due to their attractive properties of long spin dephasing times (>1 μs), long spin-polarisation lifetimes $\sim$ 5 ms [16, 17] and a triplet ground-state that can be polarized through optical pumping [6, 18, 19]. Furthermore, diamond has the highest known thermal conductivity $\sim 10^3$ $\mathrm{Wm^{-1}K^{-1}}$ and excellent mechanical properties, which obviates thermal runaway. Here we employ ensembles of optically pumped $\mathrm{NV^-}$ centres as the gain medium for a CW room-temperature maser oscillator.

The triplet ground-state ($^3A_2$) of the $\mathrm{NV^-}$ defect has a zero-field splitting D that places the quasi-degenerate $|\pm1\rangle$ sub-levels $\sim$ 2.87 GHz above the $|0\rangle$ sub-level (see Fig. 1b) [19]. At room-temperature and in zero magnetic field, the sub-levels are populated according to Boltzmann statistics, with slightly more electrons populating the lower $|0\rangle$ sub-level than the $|\pm1\rangle$ sub-levels. The triplet ground-state can be spin-polarised by pumping with optical radiation with wavelengths in the region of 532 nm [18], so that the $|0\rangle$ sub-levels become preferentially populated with respect to $|\pm1\rangle$. On photo-excitation, electrons in the $|0\rangle$ and $|\pm1\rangle$ sub-levels of the triplet ground-state undergo spin-conserving transitions into an excited triplet state (^3E). Spin-selective intersystem crossing then preferentially transfers electrons from the $|\pm1\rangle$ excited triplet-state sub-levels into a metastable singlet state, which then non-radiatively decay back to the ground-state, at roughly equal rates to the $|0\rangle$ and $|\pm1\rangle$ sub-levels. In this manner, continuous optical pumping of the $\mathrm{NV^-}$ defect centre triplet ground-state can result in spin-polarisation where up to 80% of electrons reside in the $|0\rangle$ sub-level [19].

However, stimulated emission requires a positive population inversion. This can be achieved by applying an external magnetic field along one of the four N-V defect axes (see Fig. 1a), splitting the energy of $|\pm1\rangle$ states via the Zeeman interaction and leaving the energy of the $|0\rangle$ sub-level unchanged as shown in Fig. 1c. For an electron Zeeman interaction energy, $\gamma_\mathrm{e}\hbar B$, greater than twice the zero-field-splitting energy hD (*i.e.* for $B \geq 102.5$ mT), the energy of the $|-1\rangle$ sub-level dips below that of the $|0\rangle$ state, permitting a population inversion to be established. If the transition frequency ω_s between the ground-state $|g\rangle \equiv |-1\rangle$ and excited state $|e\rangle \equiv |0\rangle$ is resonant with that of a cavity mode ω_c, then stimulated emission of microwave photons will occur. Furthermore, if the rate of stimulated emission of microwave photons exceeds the loss-rate due to cavity dissipation then build up of the cavity photon population occurs, resulting in maser oscillation.

For this study, a synthetic type-IIa diamond containing 0.36 ppm of NV^- centres was used (see Methods). The number of NV^- centres in the sample was estimated to be 7.3×10^{14}, of which one in eighteen couple to the cavity mode due to two of the three triplet sub-levels being resonant, four N-V axes and three ^{14}N hyperfine lines, yielding $N = 4.0 \times 10^{13}$ active NV^- centres. The longitudinal (spin-lattice) and transverse (spin dephasing) relaxation times were measured at 9.5 GHz and room-temperature (300 K) using electron paramagnetic resonance (EPR) spectroscopy, yielding $T_1 = 4.8$ ms and $T_2^* = 0.5$ μs respectively (see Methods). These values agree with those reported for samples with similar concentration of nitrogen [16, 17].

The 'cooperativity' $C = 4g_s^2 N/\kappa_c\kappa_s$ is a figure of merit for masers, where g_s is the single spin-photon coupling rate, $\kappa_c = \omega_c/Q$ the cavity mode decay rate, Q is the cavity quality-factor and $\kappa_s \approx 2/T_2^*$ the spin decoherence rate. For above-threshold maser oscillation the cooperativity needs to be greater than unity, $C \gg 1$. The Purcell factor is key to enhancing maser performance [2, 20] and contributes a factor g_s^2/κ_c to the cooperativity. A high Purcell factor maser cavity was therefore designed and constructed using a hollow cylindrical single-crystal sapphire ring housed within a copper cavity. The cavity supports a $TE_{01\delta}$ mode resonating at 9.22 GHz with a loaded Q-factor of 30,000. A magnetic mode volume V_m of 0.15 cm^3 was calculated, yielding a single spin-photon coupling of $g_s = 0.7$ Hz and an estimated $\sqrt{N}$-enhanced collective spin-photon coupling of $g_e = 4.4$ MHz (see Methods). This, with the cavity mode decay rate $\kappa_c \approx 1.9$ MHz and measured spin decoherence rate $\kappa_s \approx 2/T_2^* = 3.9$ MHz, yields a cooperativity $C \approx 10.6$, indicating that the maser should oscillate above a threshold pump rate per active NV^- centre of $w_{thr} \sim 300$ s^{-1} equivalent to ~ 180 mW of optical power.

The cavity was positioned between the poles of an electromagnet (Bruker) as shown in Fig. 2 and oriented horizontally to allow optical access to continuous 532 nm laser excitation. The diamond was placed inside the sapphire ring and, using EPR spectroscopy, oriented such that one set of N-V $\langle 111 \rangle$ axes was aligned parallel to the external magnetic field (see Methods and Extended Data Fig. 1). EPR spectra were collected in the dark (see Figs. 3a, 3b) then laser excitation was applied with gradually increasing power. As the laser power increases the high-field absorption lines decrease in amplitude until they disappear at a pump power of ~ 1.5 mW. This is due to equalisation of the $|e\rangle$ and $|g\rangle$ populations, *i.e.*, zero spin-polarization. Modelling of the populations under optical pumping yielded an

equalization pump rate $w_{\rm eq}$ of 1.5 $\rm s^{-1}$, corresponding to an estimated pump power of ~ 0.9 mW. Considering Fresnel and coupling losses, this agrees fairly well with the measured incident power. The low concentration of NV centres results in only 33% of the incident optical power being absorbed. Although this is far from optimal, it ensures the NV centres are pumped almost homogeneously, since the laser intensity varies marginally across the sample.

When the laser pump power was increased to 400 mW (see Fig. 3c), a cavity frequency shift of -25 MHz was observed. This was attributed to an estimated 35 °C increase in temperature of the sapphire ring and diamond, caused by heating. The observed EPR signal was a factor ~ 150 greater in amplitude than the dark state. Since the amplitude of the EPR signal is proportional to the difference in population of the $|e\rangle$ and $|g\rangle$ states (spin-polarization), it can be calibrated against the Boltzmann populated dark state to provide an estimate of the population inversion $S^z = N_{\rm e} - N_{\rm g} \approx 0.09\,N$, which agrees favourably with the predicted inversion $S^z = \kappa_{\rm c}\kappa_{\rm s}/4g_{\rm s}^2 \approx 0.10\,N$ [6]. Once the optical beam alignment and polarization were optimized for maximum emission on the high-field line and the cavity frequency had stabilized, the maser was disconnected from the EPR spectrometer and connected to a spectrum analyzer (Advantest R3271A). The magnetic field was stepped across the high-field resonances using a programmable field controller (Bruker ER-031M) and the microwave output recorded at each magnetic field position. As depicted in Fig. 4a, three separate regions of continuous maser emission – corresponding to the three hyperfine transitions – were observed. The peak maser emission power was -90.3 dBm (comparable with a hydrogen maser) with an estimated average pump rate per $\rm NV^-$ centre of $w = 410$ $\rm s^{-1}$. The maser emission persisted without degradation in power for the duration of all experiments – the longest being 10 hours – demonstrating the robustness of the system and also exhibited threshold behaviour on varying the optical pump power (See Extended Data Fig. 2a).

On the edge of the maser emission spectra (see Fig. 4b), the linewidth ~ 50 Hz approaches the Schawlow-Townes limit [21] for the observed output power: $\gamma_{\rm ST} = \frac{1}{2}\pi\hbar\omega_{\rm c}\kappa_{\rm c}^2/P_{\rm out} \approx 10$ Hz. However, near the centre of the each emission region, the maser emission line appears broadened (see Fig. 4c). Dynamical simulations of the maser cavity photon population revealed non-linear oscillations that exhibit limit-cycles [22] in the inversion–photon phase space. Further investigation revealed that they can be eliminated if the spin decay rate $\kappa_{\rm c}$

is increased (by increasing the concentration of NV centres) or if the spin-photon coupling rate g_s is decreased through detuning ($\omega_c \neq \omega_s$), which explains why limit-cycles are absent just above threshold (see Fig. 4b).

The achievement of continuous maser operation resulted from an understanding that a high Purcell factor cavity was required in combination with the narrow linewidth of transitions in a diamond containing NV^- defects. It should not be overlooked that although we used a frequency of 9.2 GHz in this study, which is close to the 9.193 GHz of a caesium atomic clock, any required frequency may be produced simply by changing the magnetic field to be resonant at the appropriate frequency. Given that the fundamental process occurring in this room-temperature continuous-wave maser is the conversion of optical photons to microwave photons, we expect that the field of diamond-based quantum optics will be an immediate beneficiary of our work, and that developments therein will form the basis for a new generation of microwave devices for applications ranging from deep-space communications to high-precision metrology.

REFERENCES

[1] Oxborrow, M., Breeze, J. & Alford, N. Room-temperature solid-state maser. *Nature* **488**, 353–356 (2012).

[2] Breeze, J. *et al.* Enhanced magnetic Purcell effect in room-temperature masers. *Nat. Commun.* **6** (2015).

[3] Salvadori, E. *et al.* Nanosecond time-resolved characterization of a pentacene-based room-temperature maser. *Sci. Rep.* **7**, 41836 (2017).

[4] Poklonski, N., Lapchuk, N. & Lapchuk, T. Inverted EPR signal from nitrogen defects in a synthetic diamond single crystal at room temperature. *JETP Letters* **80**, 748–751 (2004).

[5] Poklonski, N. *et al.* Nitrogen-doped chemical vapour deposited diamond: a new material for room-temperature solid state maser. *Chin. Phys. Lett.* **24**, 2088 (2007).

[6] Jin, L. *et al.* Proposal for a room-temperature diamond maser. *Nat. Commun.* **6** (2015).

[7] Kraus, H. *et al.* Room-temperature quantum microwave emitters based on spin defects in silicon carbide. *Nat. Phys.* **10**, 157–162 (2014).

[8] Smith, W., Sorokin, P., Gelles, I. & Lasher, G. Electron-spin resonance of nitrogen donors in

diamond. *Phys. Rev.* **115**, 1546 (1959).

[9] Sorokin, P., Lasher, G. & Gelles, I. Cross relaxation studies in diamond. *Phys. Rev.* **118**, 939 (1960).

[10] Siegman, A. *Microwave Solid - State Masers* (McGraw-Hill, 1964).

[11] Loubser, J. & van Wyk, J. Electron spin resonance in the study of diamond. *Rep. Prog. Phys.* **41**, 1201 (1978).

[12] Gruber, A. *et al.* Scanning confocal optical microscopy and magnetic resonance on single defect centers. *Science* **276**, 2012–2014 (1997).

[13] Taylor, J. *et al.* High-sensitivity diamond magnetometer with nanoscale resolution. *Nat. Phys.* **4**, 810–816 (2008).

[14] Maze, J. *et al.* Nanoscale magnetic sensing with an individual electronic spin in diamond. *Nature* **455**, 644 (2008).

[15] Childress, L. *et al.* Coherent dynamics of coupled electron and nuclear spin qubits in diamond. *Science* **314**, 281–285 (2006).

[16] Takahashi, S., Hanson, R., van Tol, J., Sherwin, M. S. & Awschalom, D. D. Quenching spin decoherence in diamond through spin bath polarization. *Phys. Rev. Lett.* **101**, 047601 (2008).

[17] Jarmola, A., Acosta, V., Jensen, K., Chemerisov, S. & Budker, D. Temperature-and magnetic-field-dependent longitudinal spin relaxation in nitrogen-vacancy ensembles in diamond. *Phys. Rev. Lett.* **108**, 197601 (2012).

[18] Robledo, L., Bernien, H., van der Sar, T. & Hanson, R. Spin dynamics in the optical cycle of single nitrogen-vacancy centres in diamond. *New J. Phys.* **13**, 025013 (2011).

[19] Doherty, M. W. *et al.* The nitrogen-vacancy colour centre in diamond. *Phys. Rep.* **528**, 1–45 (2013).

[20] Breeze, J. D. *et al.* Room-temperature cavity quantum electrodynamics with strongly coupled Dicke states. *npj Quantum Information* **3**, 1 (2017).

[21] Schawlow, A. L. & Townes, C. H. Infrared and optical masers. *Physical Review* **112**, 1940 (1958).

[22] Dimer, F., Estienne, B., Parkins, A. & Carmichael, H. Proposed realization of the Dicke-model quantum phase transition in an optical cavity QED system. *Physical Review A* **75**, 013804 (2007).

[23] Yavkin, B., Mamin, G. & Orlinskii, S. High-frequency pulsed endor spectroscopy of the NV^-

centre in the commercial HPHT diamond. *J. Mag. Res.* **262**, 15–19 (2016).

[24] Tavis, M. & Cummings, F. W. Exact solution for an N-molecule radiation-field Hamiltonian. *Phys. Rev.* **170**, 379 (1968).

[25] Carmichael, H. J. *Statistical Methods in Quantum Optics 1: Master Equations and Fokker-Planck Equations* (Springer, 2003).

[26] Manson, N. & Harrison, J. Photo-ionization of the nitrogen-vacancy center in diamond. *Diamond and related materials* **14**, 1705–1710 (2005).

[27] Aslam, N., Waldherr, G., Neumann, P., Jelezko, F. & Wrachtrup, J. Photo-induced ionization dynamics of the nitrogen vacancy defect in diamond investigated by single-shot charge state detection. *New J. Phys.* **15**, 013064 (2013).

[28] Kajfez, D. & Guillon, P. *Dielectric Resonators* (Artech House, Inc., 1964), 1st edn.

[29] Wee, T.-L. *et al.* Two-photon excited fluorescence of nitrogen-vacancy centers in proton-irradiated type Ib diamond. *J. Phys. Chem. A* **111**, 9379–9386 (2007).

ACKNOWLEDGEMENTS

We thank Dr. Jacqueline Hall and Dr. Matthew Markham of Element 6 Ltd. (UK) for supplying the diamond samples, Prof. Paul French and Prof. Roy Taylor of the Photonics Group at Imperial College for generously lending us their CW laser and Erik Bauch of Harvard University for helpful discussions. This work was supported by the UK Engineering and Physical Sciences Research Council through grants EP/K011987/1 (IC) and EP/K011804/1 (UCL). We also acknowledge support from the Henry Royce Institute.

AUTHOR CONTRIBUTIONS

J.D.B. conceived the study, developed the theory, designed the maser cavity, devised the experiment and wrote software for collecting experimental data. J.D.B. and C.W.M.K. developed the experimental design and performed experiments with input from E.S. and J.S. J.D.B. interpreted the results with input from E.S and C.W.M.K. J.S. characterised the diamond NV concentration by optical means and developed the optical pumping scheme. J.D.B., E.S. and C.W.M.K. characterised the diamonds using EPR. J.D.B. wrote the paper with assistance from C.W.M.K. and with additional editing by E.S. and N.A.

AUTHOR INFORMATION

The authors declare no competing financial interests. Readers are welcome to comment on the online version of the paper. Correspondence and requests for materials should be addressed to J.D.B. (jonathan.breeze@imperial.ac.uk).

FIGURE LEGENDS

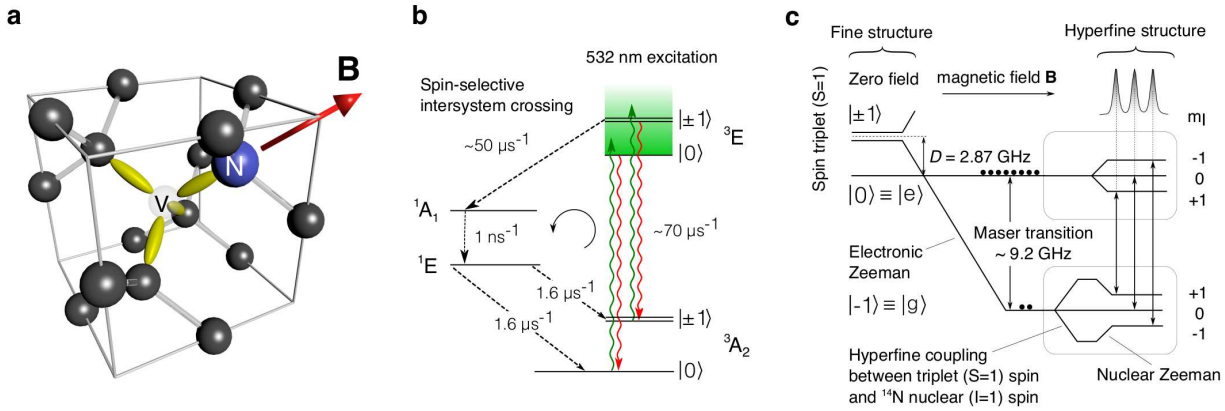

Figure 1. NV$^-$ centre structure, optical pumping and magnetic field interaction. a, The NV$^-$ centre in diamond comprises a nitrogen atom (blue) adjacent to a vacancy (light grey), surrounded by carbon atoms (black). An external magnetic field **B** (red arrow) is applied along the N-V axis. **b**, The optical spin-polarising pump process at zero-field. A continuous-wave 532 nm laser pumps electrons from the $^3A_2$ triplet ground-state into triplet excited-state ^3E via spin-conserving radiative transitions. Non-radiative spin-selective intersystem crossing transfers roughly 40% of the $|\pm1\rangle$ electrons into singlet state $^1A_1$ which decay quickly into metastable state ^1E, then back to the triplet ground-state with roughly equal probability of entering either $|\pm1\rangle$ or $|0\rangle$ sub-levels. The remaining electrons in the excited triplet state fluoresce back to the ground-state by spin-conserving radiative processes. This process preferentially populates the $|0\rangle$ sub-level producing a spin-polarized triplet ground-state [6, 18, 19]. **c**, The Zeeman and hyperfine interactions of NV centres. A magnetic field B applied parallel to the NV$^-$ axis, splits the $|\pm1\rangle$ states through the Zeeman interaction. For fields greater than $\sim$ 102.5 mT the $|-1\rangle$ state energy drops below that of the $|0\rangle$ state. If the $|0\rangle$ triplet sub-levels are preferentially populated through optical pumping, a population inversion is established. Hyperfine interaction of ($S = 1$) spin-triplets with adjacent ^{14}N ($I = 1$) nuclear spins produces three observable emission lines. The maser transition is between the $|e\rangle \equiv |0\rangle$ and $|g\rangle \equiv |-1\rangle$ states.

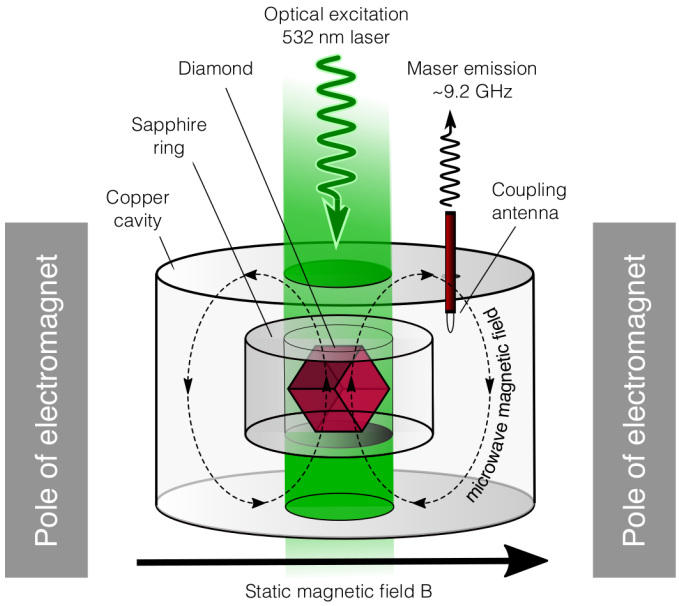

Figure 2. **Diamond maser construction.** The diamond was placed inside the sapphire ring and, using EPR spectroscopy, oriented such that one set of N-V ⟨111⟩ axes was aligned parallel to the external magnetic field (see Methods and Extended Data Fig. 1). The sapphire and diamond were housed within a cylindrical copper cavity and a microwave loop antenna coupled maser emission power into a transmission line. The diamond was optically pumped at 532 nm by a continuous-wave Nd:YAG laser.

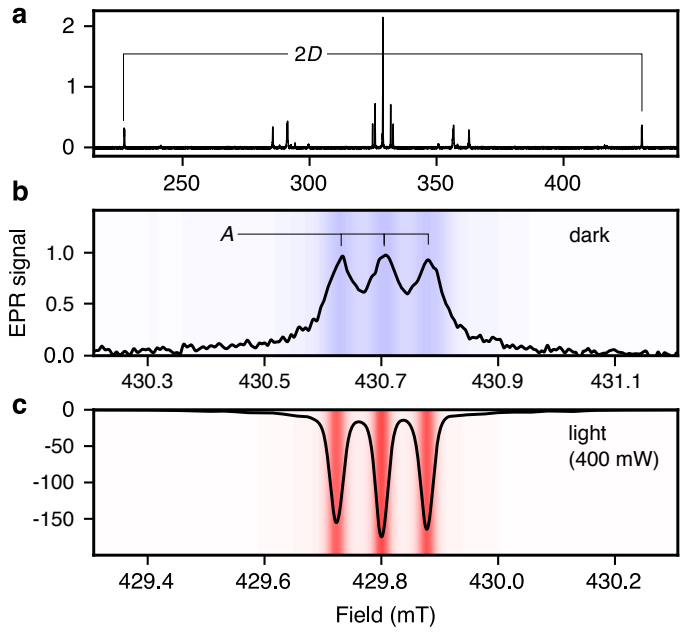

Figure 3. **Electron paramagnetic resonance spectroscopy.** **a**, Shows a wide EPR field sweep from 215 mT to 445 mT. The diamond sample was aligned to provide maximum field splitting between the low-field and high-field lines. **b**, Shows the high-field absorption in the dark state, normalised to the maximum value. The three lines are separated by ≈ 0.075 mT, due to hyperfine coupling of $(S = 1)$ triplets with adjacent $(I = 1)$ ^{14}N nuclei. **c**, The lines become emissive upon illumination by 400 mW of 532 nm laser light. The EPR signal amplitude is ~ 150 times greater than the dark-state and has shifted -25 MHz in frequency (~ 0.9 mT).

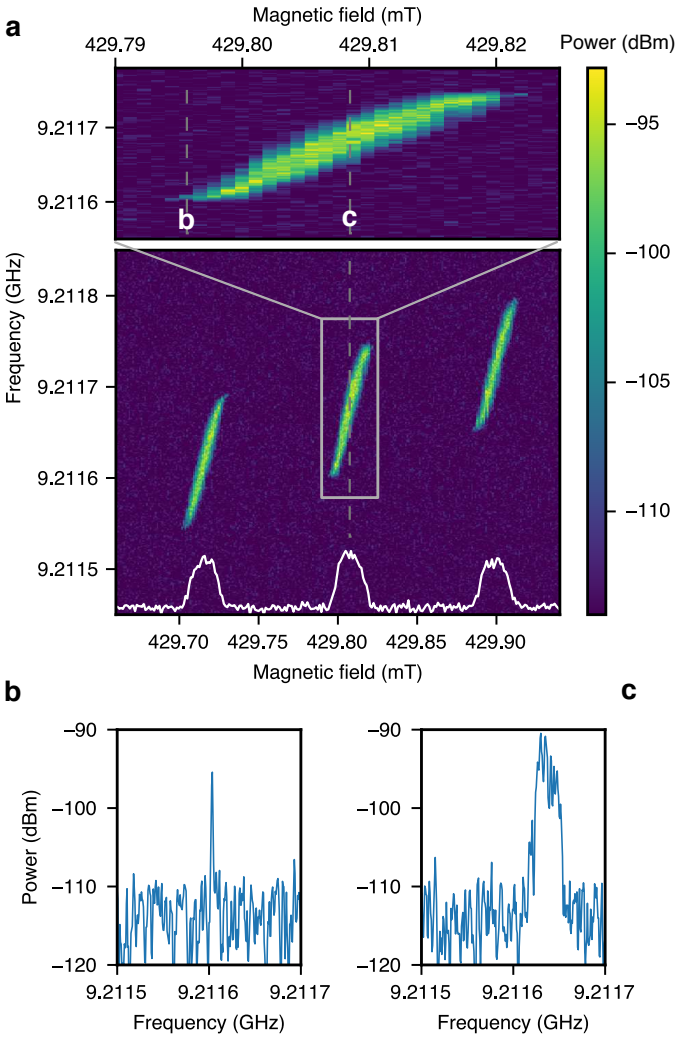

Figure 4. **Field-frequency maser emission plots.** For an optical pump power of 400 mW, the static external magnetic field was varied from 429 mT to 431 mT in 1 μT increments. At each field value, the emission spectrum emerging from the maser was recorded. **a**, This plot shows the maser emission spectrum as a function of externally applied magnetic field $\boldsymbol{B}$. There are three regions of maser oscillation corresponding to each of the hyperfine transitions. The white line shows the integrated power spectral density. The central region is magnified to show the narrow linewidth emission spectrum on the edge of threshold (**b**) and the limit-cycle broadened spectrum at the centre of the emission region (**c**). **b**, At the edge of the emission spectrum, slightly above threshold the emission has narrow linewidth ($\sim$ 50 Hz). **c**, At the centre of the emission region, the linewidth is broadened due to limit-cycles.

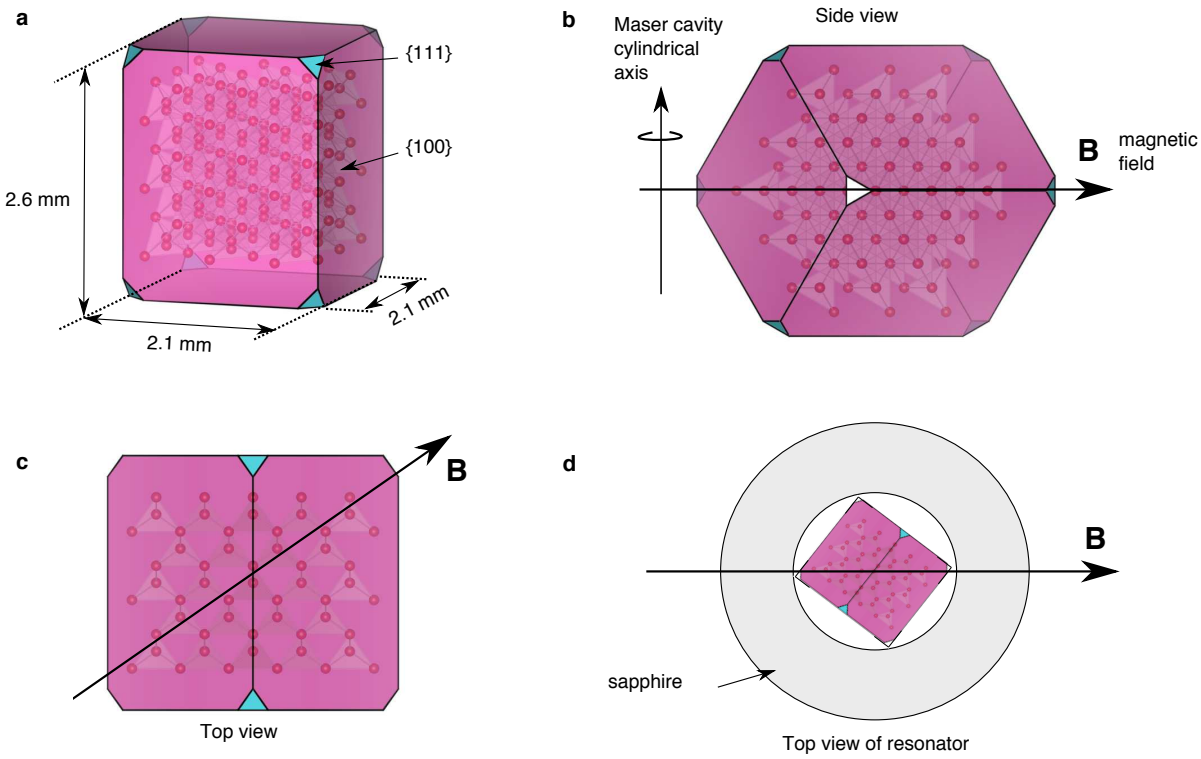

Extended Data Figure 1. **Diamond sample geometry and orientation.** **a**, The diamond is a rectangular cuboid with dimensions $2.1 \times 2.1 \times 2.6$ mm^3. The main faces (pink colour) are $\{100\}$ with the $\{111\}$ faces (to which the N–V $\langle 111 \rangle$ directions are normal) depicted in cyan for illustrative purposes. **b**, Side view of the diamond oriented within the maser cavity with static magnetic field **B** applied across the N–V $\langle 111 \rangle$ direction. The microwave magnetic field is perpendicular to the N–V defect axis and static magnetic field direction. **c**, Top view of the diamond when it is oriented inside the cavity. **d**, Top view of the diamond placed within the single-crystal sapphire ring within the maser cavity. The depiction of the structure of diamond within the crystals – carbon atoms, bonds and tetrahedra are for illustrative purposes only.

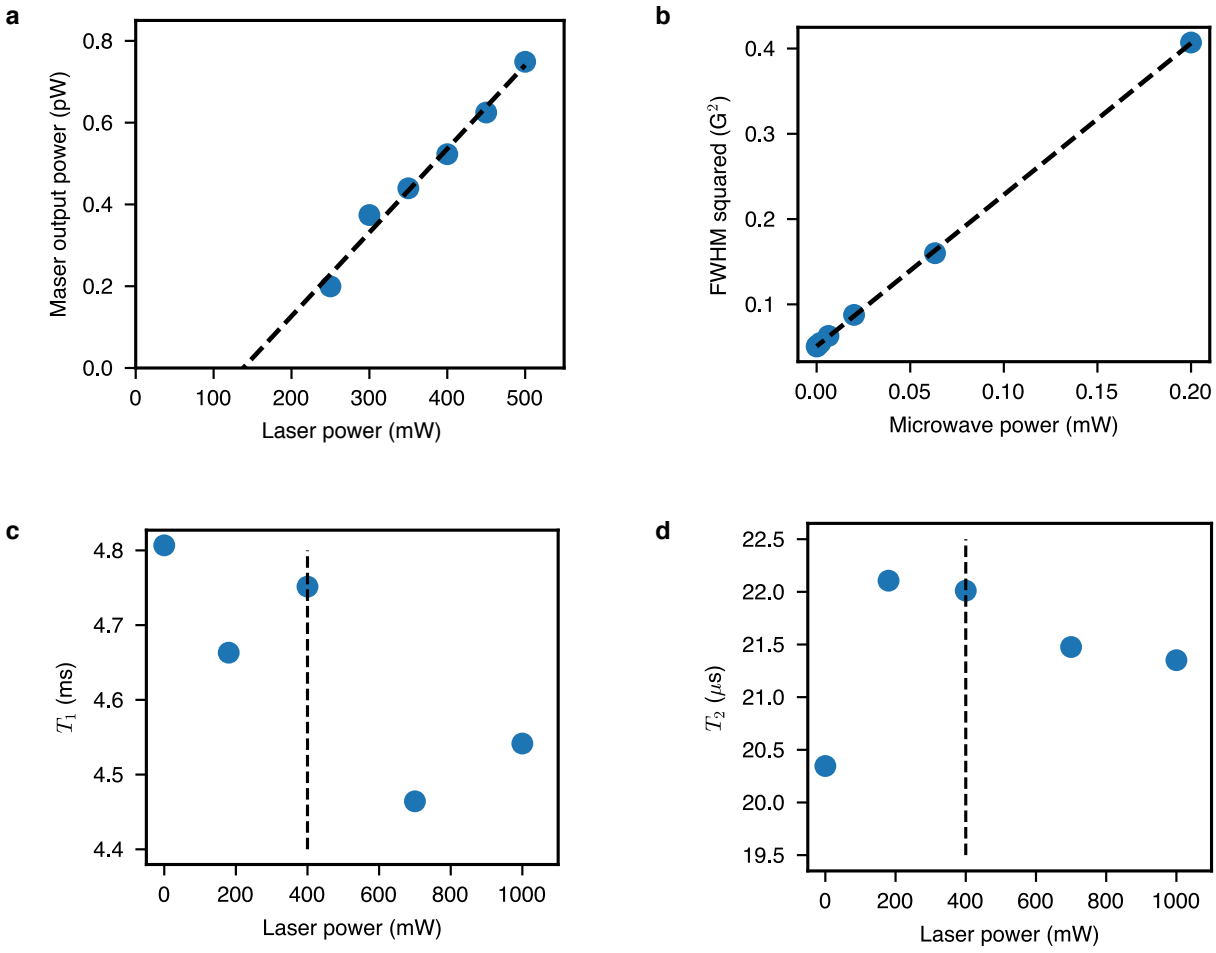

Extended Data Figure 2. **Threshold and spin relaxation measurements.** **a**, Maser threshold. The peak maser output power increases linearly as a function of the optical pump power. Extrapolation of the linear fit to zero maser output power reveals a threshold optical pump power of 138 mW, which is lower than the predicted 180 mW. **b**, Power saturation broadening. The inhomogeneous spin decoherence time $T_2^* = 2/\kappa_s$ was inferred from power saturation broadening measurements of the spin resonance lines using a continuous-wave electron paramagnetic resonance spectrometer (Bruker EMX with ER 4122HQE resonator). The spectral FWHM γ was measured as a function of interrogating microwave power. A spin decoherence rate $T_2^* = 0.52$ μs was extracted by extrapolating the square of the FWHM linewidth down to zero microwave power. **c**, Spin-lattice relaxation time T_1 as a function of laser pump power. The slight decrease in T_1 is expected and due to an increase in temperature caused by the non-radiative (heating) processes during the N–V spin-polarizing optical pump cycle. **d**, Spin-decoherence time T_2 as a function of laser pump power. There is little change in T_2, with a slight jump upon applying optical pumping, probably due to an increase in EPR signal amplitude and hence less error. There is subsequently a slight decrease due to temperature increase and pumping decoherence. Photo-conversion of $NV^- \leftrightarrow NV^0$ could also be an additional source of decoherence.

METHODS

Spin Hamiltonian. The spin-Hamiltonian for NV^- centres in diamond is given by [23]:

$$H_{\text{spin}} = \gamma_{\text{e}} \boldsymbol{S} \cdot \boldsymbol{B} - \gamma_{\text{n}} \boldsymbol{I} \cdot \boldsymbol{B} + D \left[S_z^2 - \tfrac{1}{3} S \left(S + 1 \right) \right] + \boldsymbol{S} \cdot \boldsymbol{A} \cdot \boldsymbol{I} \tag{1}$$

where γ_{e} and γ_{n} are the gyromagnetic ratios of electrons and nuclei respectively, $D \approx 2.87$ GHz is the fine structure zero-field splitting, $\boldsymbol{S}$ and $\boldsymbol{I}$ are the triplet spin and ^{14}N nuclear spin eigenvectors, $\boldsymbol{A}$ is the uniaxially anistropic hyperfine coupling tensor ($A_\perp = -2.7$ MHz, $A_\parallel = -2.1$ MHz with respect to N-V axis) and $\boldsymbol{B}$ is the magnetic field.

Spin-photon maser dynamics. The maser is modelled as an ensemble of N two-level quantum emitters (lower state $|g\rangle \equiv |-1\rangle$ and upper state $|e\rangle \equiv |0\rangle$) resonantly coupled to a cavity mode. The distance between the emitters is much less than the cavity mode wavelength and their spin-photon coupling is assumed to be homogeneous. This interaction can be described by the Tavis-Cummings Hamiltonian [24] within the rotating wave approximation:

$$H_{\text{TC}} = \hbar \omega_{\text{c}} a^\dagger a + \frac{1}{2} \hbar \omega_{\text{s}} S^z + \hbar g_{\text{e}} \left(S^+ a + a^\dagger S^- \right), \tag{2}$$

where $g_{\text{e}} = g_{\text{s}} \sqrt{N}$ is the enhanced collective spin-photon coupling strength, g_{s} is the single spin-photon coupling strength, ω_{c} is the cavity frequency, ω_{s} is the spin (two-level) transition frequency, $a^\dagger$ (a) are the cavity photon creation (annihilation) operators, S^z is the collective inversion operator and $S^\pm$ are the normalized collective spin operators. The single spin-photon coupling can be written [25, Chapter 7]:

$$g_{\text{s}} = \gamma_{\text{e}} \sqrt{\frac{\mu_0 \hbar \omega_{\text{c}}}{2 V_{\text{m}}} \frac{\kappa_{\text{s}} / (\kappa_{\text{s}} + \kappa_{\text{c}})}{1 + \Delta^2}}, \tag{3}$$

where $\Delta = 2(\omega_{\text{c}} - \omega_{\text{s}}) / (\kappa_{\text{s}} + \kappa_{\text{c}})$ is a spin-cavity detuning parameter. The Hamiltonian, coupled with a dissipative Liouvillian permits Lindblad master equations to be developed for the expectation values of the cavity field operator a, inversion S^z and transverse spin $S^\pm$ operators [25]. These can can be solved in the steady state, leading to a simple maser threshold pumping rate per NV centre:

$$w_{\text{thr}} = \gamma \left(C - 1 \right)^{-1} \eta \tag{4}$$

where $C = 4 g_{\text{s}}^2 N / \kappa_s \kappa_c$ is the cooperativity, $\gamma = 1/T_1$ is the spin-lattice relaxation rate and η is a scaling factor based on the number of photons required to increase the inversion by

one. The scaling factor η can be derived from the steady-state optical pump rate equations. We derived a value of $\eta \approx 14.4$. It holds for pump rates up to $w_{\rm thr}$ where the populations of the $|\pm 1\rangle$ states are approximately equal. This is the maser amplification regime where the inversion, given by $S^z = wN/(w + \eta\gamma)$, is positive. Accessing this regime is not challenging since the dark-state populations of the triplet ground-states have approximately equal Boltzmann populations, only requiring weak optical pumping in order for the inversion to become positive. One noticeable aspect of the threshold equation is that $w_{\rm thr}$ is lower than the scaled spin-lattice relaxation rate $\gamma\eta$ if $C > 1$, which can be considered the condition for masing. The inversion in the maser oscillation regime:

$$S^z = N_{\rm e} - N_{\rm g} = \kappa_{\rm s}\kappa_{/rmc}/4g_{\rm s}^2 = N/C \tag{5}$$

is always less than N when $C > 1$. Above threshold and for stready-state conditions, we solve a non-linear system of rate equations comprising seven NV^- states (triplet ground, triplet excited and singlet), a cavity field operator $\hat{a}$, a longitudinal (inversion) operator $\hat{S}^z$ and a transverse spin operator $\hat{S}^-$. These equations are the Maxwell-Bloch equations coupled to a set of optical spin dynamical rate equations.

Diamond preparation and characterisation. A synthetic diamond with natural carbon isotopic abundance, doped with ~ 5 ppm of nitrogen donors was grown by chemical vapour deposition. The diamond was irradiated by 4.5 MeV electrons, equivalent to a dose of 5×10^{18} cm^{-2} to create vacancies. It was then annealed for 2 hours at 400 °C, 16 hours at 800 °C and a further 2 hours at 1200 °C to promote the formation of nitrogen-vacancy defect centres. The diamond was laser cut into a cuboid of dimensions $2.1 \times 2.1 \times 2.6$ mm^3 with $\{100\}$ faces and $\langle 111\rangle$ crystal directions (along which the NV centres lie) emerging from the corners of the cuboid. These steps were performed by Element 6 (UK). The diamond was cleaned in nitric acid to remove residual graphitic carbon (48 hours) then polished using a lint-free cloth.

Nitrogen-vacancy (NV) defect centres exist in neutral NV^0 and charged NV^- states. Using UV-Vis absorbance spectroscopy (Cary 5000 UV-VIS-NIR spectrophotometer, Ocean Optics USB 2000+ fiber optic spectrometer), the NV^- concentration in the sample was found to be 0.36 ppm. Further photoluminescence (PL) studies revealed that the ratio of charged to neutral NV centres (NV^-/NV^0) was ≈ 0.55 under illumination from a 100 mW CW 532 nm Nd:YAG laser. Furthermore, the ratio decreased slightly as the laser power

was reduced, suggesting that some NV^- had been photo-converted into NV^0 [26, 27]. The total concentration of NV^0 and NV^- was [NV] $\approx$ 1 ppm, which given the initial nitrogen concentration of $[N^0] \approx 5$ ppm, equates to a N-to-NV conversion efficiency of 20%. The final nitrogen (P1 centre) concentration would be $[N^0] \approx 4$ ppm in this case.

EPR spectroscopy of NV centres. EPR spectroscopy (Bruker Elexsys E580 spectrometer with ER 4118 X-MD5 resonator) at 9.5 GHz was employed to align the diamond sample and measure the relaxation times T_1, T_2 and T_2^* of the high field line. The diamond was held inside a hollow low-loss quartz tube and oriented inside the cylindrical single-crystal sapphire ring of the resonator so that two N-V axes lay in a plane perpendicular to the cylindrical axis. The diamond was rotated about the cylindrical axis of the cavity until the external magnetic field was aligned with one of the two $\langle 111 \rangle$ directions and colinear with a N-V defect axis. This was achieved by sweeping the magnetic field from 200 mT to 450 mT and noting the minimum and maximum fields at which absorption/emission occurred. When the difference in magnetic field between the low-field and high-field lines was equal to twice the zero-field splitting $4\pi D/\gamma_e$ or 205 mT, the absorption peaks associated with the other three $\langle 111 \rangle$ directions coalesced, becoming quasi-degenerate at $\sim$ 370 mT. Pronounced low-field absorption and high-field emission peaks appeared at 239 mT and 444 mT respectively. Nitrogen spin-$\frac{1}{2}$ (P1) impurities were evident at 341 mT. The spin-lattice relaxation time (T_1) was measured using an inversion recovery sequence $\pi - T - \pi/2 - \tau - \pi - \tau -$ echo, where the interpulse delay τ was kept fixed at 1.2 μs and the time interval T was incremented in steps of 10 μs from an initial value of 1 μs. The $\pi/2$ pulse length was 200 ns and each data set comprised 1024 points. The magnetic field was set on resonance with the $m_I = 0$ hyperfine line of the highest EPR band (see Figure 1c). The homogeneous spin relaxation time (T_2) was measured with a Hahn echo sequence $\pi/2 - \tau - \pi - \tau -$ echo, where the interpulse delay τ was incremented in steps of 80 ns from an initial value of 1.2 μs. The inhomogeneous spin dephasing time T_2^* was measured using the saturation broadening technique. The $m_I = 0$ linewidth was measured as a function of applied microwave power. By extrapolating a linear fit of linewidth squared versus microwave power down to zero power, the inhomogeneous broadening and hence T_2^* can be found (see Supplementary Information for more details).

Maser cavity. A high Purcell factor cavity was designed using a radial mode-matching technique [28]. The cavity comprised a single-crystal sapphire dielectric ring resonator ($\varepsilon =$

9.394, outer diameter 10 mm, inner diameter 5.1 mm and height 6.5 mm) housed centrally within an oxygen-free high-conductivity copper cavity (diameter 36 mm and height 28 mm). The cavity supported a $TE_{01\delta}$ mode resonating at 9.22 GHz with an unloaded Q-factor of 55,000. The central bore containing the diamond had an electric filling factor of 0.008, allowing the dielectric properties of the diamond to be neglected. A magnetic mode volume $V_{\rm m}$ of 0.15 cm^3 was calculated from the ratio of the stored magnetic energy within the cavity to the maximum magnetic field energy density, $V_{\rm m} = \int_{\rm V} |\mathbf{H}(\mathbf{r})|^2 dV / |\mathbf{H}(\mathbf{r})_{\rm max}|^2$. The electric filling factor of the sapphire was 0.76 and the magnetic filling factor of the central hole was 0.14. The diamond was mounted inside the sapphire resonator and held in place by quartz tubes. Coupling to the cavity was achieved by a small adjustable antenna loop, set slightly below critical coupling ($k = 0.85$) to yield a loaded Q of 30,000.

Optical pumping. A continuous-wave 532 nm laser was used to pump the NV^- centres (Laser Quantum Finesse Pure) with spot size 2.5 mm. The laser beam was adjusted until it was colinear with the cavity axis and p-polarized with respect to the surface of the diamond, since the angle of incidence was close to the Brewster angle (67.2°). The one-photon absorption cross-section of NV^- centres at 532 nm is $\sigma = 3.1 \times 10^{-17}$ cm^2 [29]. The power required to pump the NV centres at rate w is therefore $P_{\rm p} \approx w\hbar\omega_{\rm p}(A/\sigma)$, where $\omega_{\rm p}$ is the pump frequency and A is the area (spot-size). The defect pump rate $w = \sigma I/\hbar\omega_{\rm p}$, where ω_p the optical pump frequency, is proportional to the local pump intensity $I = P_{\rm p}/A$ which varies across the sample.